High-Frequency Microwave Emission of a Trilayer Magnetic Tunnel Junction in the Absence of External Magnetic Bias Field

R.N.S. Rajapakse,[1] Z.M. Zeng,[2] and H.W. Jiang[1,*]

[1] *Department of Physics and Astronomy, University of California, Los Angeles, California 90095, USA*

[2] *Key Laboratory of Multifunctional Nanomaterials and Smart Systems, Suzhou Institute of Nano-tech and Nano-bionics, Chinese Academy of Sciences, Ruoshui Road 398, Suzhou 215123, P. R. China*

(Received 13 January 2020; revised 7 May 2020; accepted 23 June 2020; published 14 July 2020)

We perform an experimental study of dc-current-induced microwave emission in a magnetic tunnel junction (MTJ) consisting of three active magnetic layers. In this trilayer structure, in addition to a conventional bilayer orthogonal MTJ containing a perpendicular free layer and an in-plane fixed layer, a second perpendicular layer is introduced. We find that the microwave emission frequency induced by spin-transfer torque can reach as high as 6 GHz in the absence of any applied magnetic field. Moreover, microwave emission is observed for both current polarities, where a redshift is seen with an increase in the magnitude of the current. We discuss the spin dynamics of the observed bidirectional high-frequency emission and the physical origin of the redshift. The distinct microwave emission properties exhibited by this trilayer MTJ structure could potentially be useful for future applications in nanoscale spintronic devices in fields such as microwave communication and neuromorphic computing.

DOI: 10.1103/PhysRevApplied.14.014040

I. INTRODUCTION

The injection of a spin-polarized current into a nano-sized magnet can excite steady-state magnetization precession via spin-transfer torque (STT) [1,2], and, with tunneling magnetoresistance (TMR), this can be captured as an electrical signal measurable at the electrodes. Spin-transfer-torque nano-oscillators (STNOs) [3–6] utilizing these phenomena have attracted great attention as future nanoscale microwave devices due to their scalability, high frequency tunability, broad range of working temperature, and high compatibility with existing semiconductor manufacturing processes [7–11]. These promising devices have developed tremendously over the past few years in many respects; for example, the output power has been enhanced [12–15] and the linewidth has been improved [16–19]. One of the major efforts has been an attempt to eliminate the need for an external bias field [20–24] but still to achieve a reasonable output microwave frequency in the interest of practical applications. Recently, STNOs have attracted even more attention as building blocks for neural networks to be used in computational tasks for artificial intelligence [11,25–28]. These emerging new avenues for STNOs in contemporary research fields have further demonstrated their promise in future technology.

Commonly, STNOs are formed with a pinned polarization layer and a free precessing layer, where STT-induced emission can be obtained only for one current direction [5]. We report STT-induced microwave emission from a magnetic tunnel junction (MTJ) consisting of three active magnetic layers, where an additional perpendicular layer is introduced as the third layer on top of an otherwise conventional stack. We find that the emission frequency can reach as high as 6 GHz in the absence of any external field due to the enhanced interfacial perpendicular magnetic anisotropy [29,30] (IPMA) in the middle layer owing to the additional $Co_{20}Fe_{60}B_{20}$/MgO interface introduced along with the top layer. Another unique feature of this STNO is that STT microwave emission can be realized for both current polarizations due to the dual polarizer action of the top and bottom layers. Our experiments with this STNO in a magnetic field show the spin dynamics of the oscillator to be that of out-of-plane (OOP) modes induced in the middle layer. These functionalities of the trilayer STNO could potentially be useful in an array of applications in fields such as microwave communication, neuromorphic computing, and artificial intelligence.

II. DEVICE AND CHARACTERIZATION

The structure of the MTJ presented in this paper can be described as substrate/buffer layer/PtMn(20)/$Co_{70}Fe_{30}$(2.3)/Ru(0.85)/$Co_{60}Fe_{20}B_{20}$(2.7)/MgO(0.8)/$Co_{20}Fe_{60}B_{20}$(1.4)/MgO(0.85)/$Co_{20}Fe_{60}B_{20}$(1.5)/capping layer, where the thicknesses in the parentheses are in nanometers. In fabricating the devices, films are deposited using a

*jiangh@physics.ucla.edu

Singulus TIMARIS PVD system and annealed at 300 °C for 2.0 h in a magnetic field of 1 T perpendicular to the film plane. The films are then patterned into nanopillars with different aspect ratios using electron-beam-lithography and ion-milling techniques. All results presented in this paper are obtained at room temperature for a single circular device with a diameter of 100 nm. Electrical contacts with the device are made using a high-bandwidth (40 GHz) microwave probe, and the microwave emission is recorded directly by a 26-GHz spectrum analyzer through a bias tee and with an amplification of 28 dB. The complete experimental setup is presented in Fig. S1 of the Supplemental Material [31]. In the following sections, the emission power presented (unless expressed in arbitrary units) is corrected for this amplification and the transmission inefficiency due to the impedance mismatch between the device and the rest of the circuit, as described in Sec. V of the Supplemental Material, where the impedance of the MTJ is approximated by its resistance [31].

As shown in Fig. 1(a), the device can be understood as being composed of three principal magnetic layers, referred to as the top, middle, and bottom layers, where the bottom layer is the top section of a synthetic antiferromagnetic layer [32], usually referred to as the "reference layer." The Fe-rich $Co_{20}Fe_{60}B_{20}$ in the middle and top layers is used to create a stronger IPMA at the $Co_{20}Fe_{60}B_{20}$/MgO interface [30]. The two tunnel junctions corresponding to each MgO barrier form two resistors that are connected in series, as shown on the right-hand-side of Fig. 1(a); therefore, the total resistance of the MTJ is the sum of the values of these individual resistances. In this study, a positive current is defined to be one with electrons flowing from bottom to the top layer. The convention for the coordinate system for the optional external magnetic field is shown in Fig. 1(a). A perpendicular-magnetoresistance (MR_Z) loop obtained at 10 μA is shown in Fig. 1(b), where the insets illustrate individual magnetization configurations at different points. Two piecewise linear segments are present, in between which two hysteresis transitions occur. The low TMR variation seen in both the linear segments and the transitions suggests that the magnetizations in the trilayer maintain close mutual angles throughout the MR_Z loop, including the major reorientation (switching).

The top- and middle-layer thicknesses are well below the threshold required to induce a perpendicular easy axis via IPMA [30], while the bottom layer is a well-established in-plane reference layer [32–34]. Within the field range studied (150 mT for B_Z), the bottom layer is expected to be affected minimally by the external field. The magnetization in the top layer is expected to be normal to the film plane, while that in the middle layer is expected to be canted away from the vertical axis due to dipole coupling from the bottom layer. In a conventional bilayer MTJ, the canting angle is about 10° [35]; however, the canting angle here is expected to be much less, due to the high IPMA

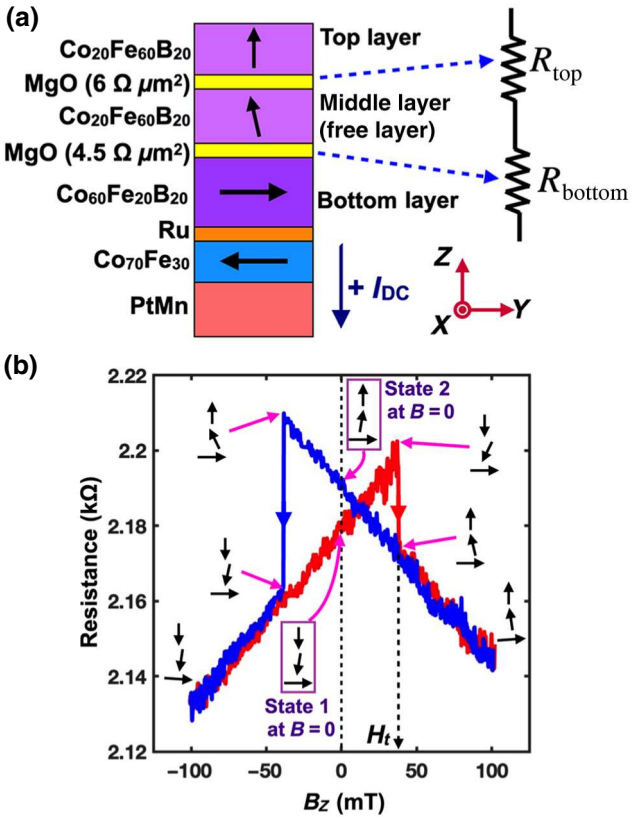

FIG. 1. Structure and characterization of the MTJ. (a) Schematic diagram of the MTJ at zero bias field. The left part represents the key layers of the design, while the right part represents the corresponding electrical-circuit model. The device consists of three layers, referred to as the top, middle, and bottom layers. The top and middle layers possess a perpendicular easy axis, while the bottom layer possesses an in-plane easy axis. The conventions for the coordinate system and for a positive current are also shown. (b) Magnetoresistance curve for a fixed bias current (10 μA) and a perpendicular magnetic field. The insets illustrate the magnetization orientations in the three layers, explaining the linear segments and the hysteresis transitions. The red and blue curves correspond to sweeping the field up and down, respectively. As shown, the zero-field configuration can be initialized to either state 1 or state 2 by applying a negative or positive large field. The definition of the right-hand transition field, H_t, is shown.

field from the dual $Co_{20}Fe_{60}B_{20}$/MgO interfaces and the vertical dipole coupling from the top layer. (This canting angle is exaggerated in the figures for clarity.) As shown in Fig. 1(b), the zero-field configuration of the MTJ can be initialized in two different states, namely, state 1 and state 2. Here, state 1 (state 2) is the configuration with both the top and the middle magnetizations prepared to point downwards (upwards). State 1 (state 2) can be realized by applying a large negative (positive) B_Z prior to the experiment. The observed linear segments result from minor variations of the canting angle of the middle layer, while

the hysteresis transitions are due to switching of the top and middle layers. The field at which the right-hand side transition occurs is denoted by H_t [Fig. 1(b)] for later reference. MR_X and MR_Y loops are also obtained (see Fig. S2 of the Supplemental Material [31]).

III. MICROWAVE EMISSION MEASUREMENTS

Microwave emission in the absence of any external field is recorded for both current directions, with simultaneous resistance measurements. Figures 2(a) and 2(b) represent the recorded emission, the calculated power delivered to a matched load, and the simultaneous device resistance. Figures 2(c) and 2(d) present individual spectra for selected positive and negative current values, respectively, where the curves are vertically shifted by 40 nW GHz^{-1} for clarity. Prior to recording of the emission, the device is initialized in state 2, after which the current is swept along $+I_{dc}$ followed by a $-I_{dc}$ sweep. At a certain $-I_{dc}$, the device undergoes current-induced switching (CID) into state 1, as is evident from the slight discontinuity appearing on the left branch. Through the remainder of the recording, the device remains in state 1; however, if the current continues to increase along $+I_{dc}$, a similar discontinuity appears (not shown) on the positive branch, indicating CID from state 1 back to state 2.

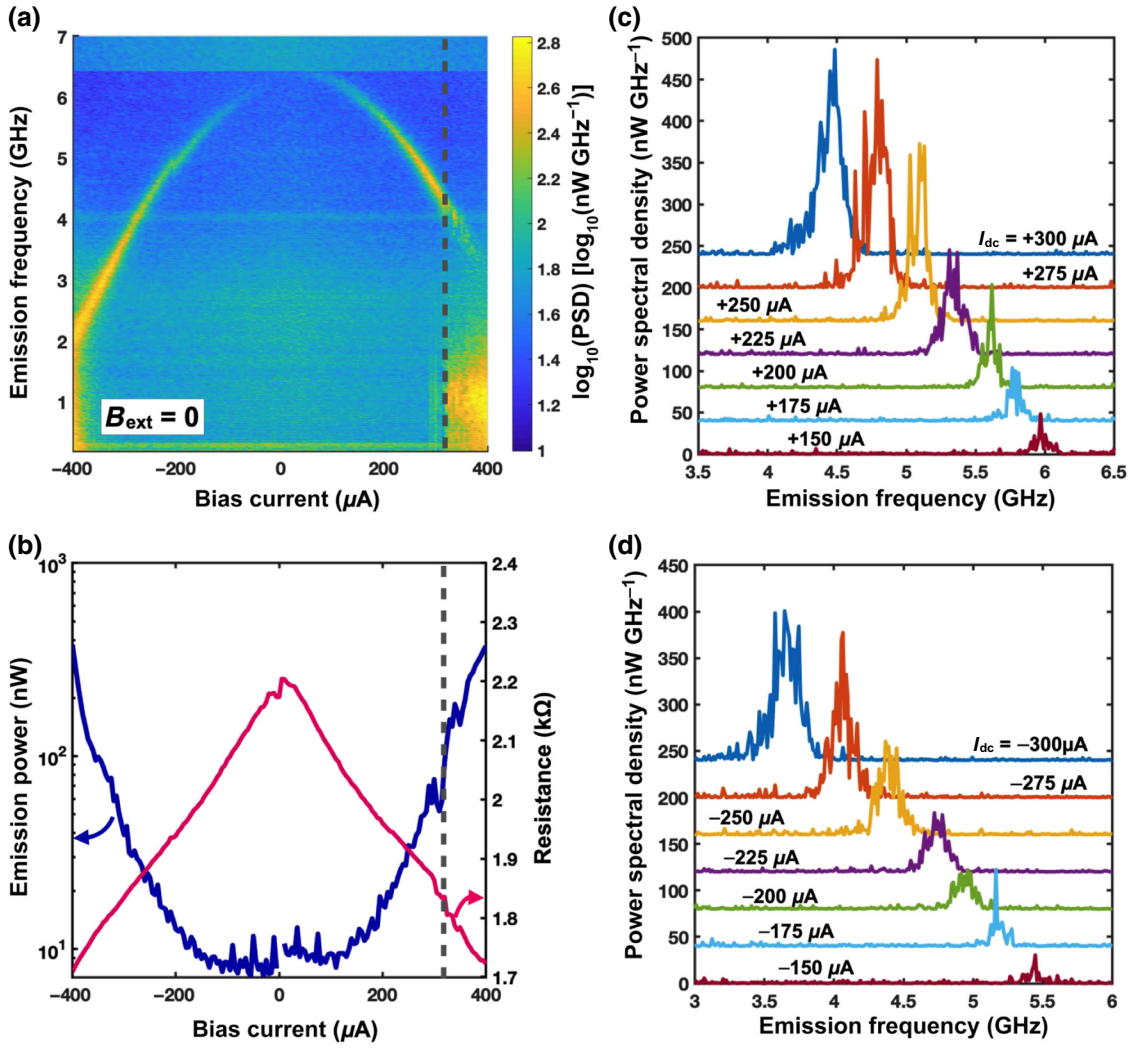

FIG. 2. Microwave emission at zero bias field. (a) Microwave emission spectrum for both current directions obtained at zero external magnetic field. Starting from about 6 GHz, a redshift is observed for both current polarities, where the emission becomes highly incoherent beyond $+320$ μA and -400 μA. PSD, power spectral density. (b) Integrated power delivered to a matched load (blue line, left axis) and resistance measured simultaneously during the experiment (pink line, right axis). The dashed line is a guide for identifying the simultaneous footprints of the onset of incoherent emission in the positive current direction. As can be seen, the resistance changes by more than 15% within the coherent-oscillation region for both current polarities. (c),(d) Emission spectra for selected positive and negative bias-current values, respectively, where the curves are vertically offset by 40 nW GHz^{-1} for clarity.

The emission spectrum resembles an inverted parabolic shape slightly shifted towards the positive current direction. The emission builds up for both positive and negative I_{dc}, with a redshift up to a certain point, beyond which highly incoherent oscillations start to occur, as indicated by the sudden broadening in the emission peak. Within the region of coherent oscillation, the emission power increases beyond 90 nW for both current directions; this emission power is about two orders of magnitude greater than what thermally induced emission can offer [36] for MgO-based MTJs, suggesting the occurrence of STT-induced oscillations for both current directions. Furthermore, within this coherent-emission region, for both positive and negative I_{dc}, the device resistance drops by more than 15% of its zero-field value [Fig. 2(b)], revealing a considerable tilting of the precessing magnetization away from its equilibrium axis. This fact further validates the prediction that the emission (for both positive and negative I_{dc}) is STT-induced rather than thermally induced, where such a drop in resistance cannot be expected.

For a perpendicular precessing layer, the oscillation frequency is directly proportional to the local effective field, i.e., the internal field (B_{int}) [5]. The fact that the two sides of the emission parabola are connected smoothly across zero current suggests that the same layer (either the top or the middle layer) produces the emission for both positive and negative I_{dc}. To further investigate the oscillating layer and its modes, the response of the emission from the device to an external field is studied. An important clarification to be made here is that the purpose of using this external field is to observe its effect on the precessional cone and the emission frequency; the device is otherwise capable of producing emission at zero field. An interesting distinction in the response is observed between initialization in state 1 and in state 2. Results recorded at a fixed bias of $+150$ μA are presented in Figs. 3(a) and 3(b) for initialization in state 1 and state 2, respectively. For initialization in state 1, as B_Z is swept in the positive direction, a linear redshift is observed up to a critical field, where a discontinuous transition occurs to a higher frequency, which is then followed by a continuous linear blueshift. In contrast, for initialization in state 2, only the blueshift is present from the very beginning. Apart from this, the power is observed to increase with the redshift but to decrease with the blueshift. It turns out that both of these observations can be explained by OOP oscillations induced in a perpendicular free layer. Given that both the top and the middle layers are perpendicular, the question is which of those two is in fact producing the observed microwave output. The possibility of the top layer producing the observed emission is eliminated due to the lack of an appropriate neighboring reference layer. In contrast, for the middle layer, an in-plane bottom layer is present, which can successfully capture the dynamical TMR during OOP precession in the former layer.

Considering the OOP precessional modes in the middle layer, the observations in Fig. 3 can be explained as follows. When the device is in state 1 with a field applied upwards, the magnitude of B_{int} in the middle layer is $\mu_0(H_k - M_s)m_z - B_Z$, where H_k, M_s, m_z, and B_Z are the IPMA field, saturation magnetization, vertical magnetization component, and external field, respectively.

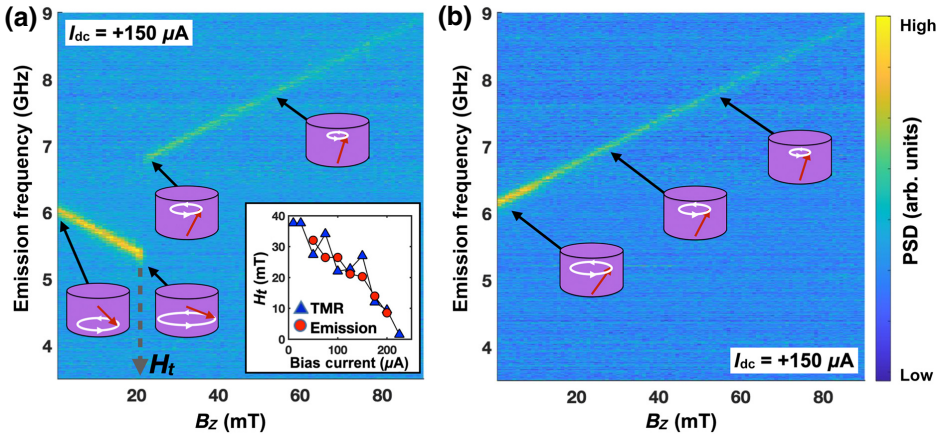

FIG. 3. Oscillation modes in middle layer and their response to an external field. (a) Manipulation of emission with a vertical external field ($+B_Z$) at a fixed bias current of $+150$ μA after initialization in state 1. The insets illustrate the evolution of the cone angle, where the effect is exaggerated for clarity. In state 1, the middle layer starts to precess with a downward cone, which undergoes field-induced switching (FIS) at a critical field. The definition of this transition field H_t is shown. During this reorientation, a discontinuous frequency jump occurs, followed by a monotonic blueshift. The inset graph shows the correlation between the transition field for FIS for different bias currents derived from this emission-cone-flipping method and magnetoresistance measurements as defined in Fig. 1(b). (b) Manipulation of emission after initialization in state 2 (bias current, $+150$ μA). In state 2, the middle layer starts to precess with an upward cone, and no FIS occurs, leading to a monotonic blueshift.

For state 2 with B_Z remaining upwards, this is modified to $\mu_0(H_k - M_s)m_z + B_Z$. An increase in B_{ext} decreases the magnitude of B_{int} in the former case, while the opposite occurs in the latter case. Since the oscillation frequency is directly proportional to B_{int}, the redshift branch in Fig. 3(a) can thus be explained. At the end of this redshift, the device undergoes field-induced-switching (FIS), after which the oscillation cone points upwards, where B_{int} now increases with B_Z, leading to the observed blueshift. The field at which this FIS occurs, paving the way to the blueshift branch, is denoted by H_t. In Fig. 3(b), in contrast, the device starts off in state 2 (cone upwards), and hence no FIS occurs, explaining the monotonic blueshift with B_Z.

Since I_{dc} is held constant, the observed increase (decrease) in emission power with the redshift (blueshift) suggests an increase (decrease) in the dynamical TMR during precession [5], meaning an increase (decrease) in the cone angle. Such an increase (decrease) in the cone angle decreases (increases) m_z, leading to a decrease (increase) in B_{int}, which further enhances the existing redshift (blueshift). However, this contribution from the evolution of the cone angle is expected to be dominated by that from the change in B_{int}. The behavior of the precession cone during a B_Z sweep is illustrated in the insets in Figs. 3(a) and 3(b). The cone axis is taken to be vertical for simplicity, and the variation of its angle is exaggerated for clarity.

Occurrences of this discontinuity (in state 1) for different values of I_{dc} are also recorded (see Fig. S4 of the Supplemental Material [31]). Furthermore, MR_Z loops for different values of I_{dc} are obtained (see Fig. S3 of the Supplemental Material [31]). In both cases, corresponding H_t values are derived as defined in Figs. 1(b) and 3(a). It turns out that H_t derived via both of these methods decreases with increasing I_{dc} as, with an increase in I_{dc}, STT rotates the magnetization further away from the vertical axis, hence facilitating the completion of the switching at a lower external field than would otherwise be the case. In fact, it is found that for I_{dc} greater than 200 μA, only the continuous blueshift is present even after initialization in state 1, indicating the current itself completes the switching without the aid of any external field. A comparison of values of H_t derived by these two independent methods demonstrates good correlation, as seen in the inset of Fig. 3(a), suggesting that the specific event shown in Fig. 3(a) directly corresponds to a switching event on the MR_Z loop, further validating the OOP-oscillation model.

IV. DISCUSSION

In conventional bilayer STNOs, for one current polarity, STT acts as an antidamping torque, while for the other it acts as an additional damping torque [1,2], hence leaving room for persistent STT oscillations in only the former case, given that the threshold magnitude of the current is met. In our device, the top and bottom layers are considered to have hybrid roles that facilitate the observed bidirectional emission. Computational studies [37] on a bias-field-free STNO with an in-plane polarizer and a perpendicular precessing layer have found, for the parameters of a typical MTJ, that bias-field-free emission can be realized when a fieldlike torque is present and its ratio to the STT has a negative value. Given this scenario, the perpendicular middle layer of the trilayer device experiences a damping (antidamping) STT caused by the bottom layer when electrons pass through the bottom (middle) layer to the middle (bottom) layer. In the meantime, the STT from the top layer creates a damping (antidamping) effect on the middle layer when electrons pass through the top (middle) layer to the middle (top) layer. This is summarized in the insets of Fig. 4. The strengths of such damping and antidamping torques depend on the instantaneous magnetization direction and the orientation of the cone itself, which vary with the current direction. Therefore, under the right quantitative conditions, sustainable oscillations can be expected to occur owing to an overall net antidamping effect for both current directions.

One piece of evidence for such a dual-polarizer action is the difference between the critical currents for each polarity as demonstrated in Fig. 4. Here, the critical currents are derived from a linear fit to the inverse power plotted against the bias current in the subcritical regime [38]. The estimated critical currents for positive and negative polarities are about $+128$ μA and -110 μA, respectively. The critical current for positive I_{dc} is about 16% larger than that for positive I_{dc}, which is consistent with the active-polarizer assignment (see the insets of Fig. 4). For positive I_{dc}, the top layer creates antidamping, but this is not expected to be as strong as the effect of the bottom layer, which is a well-established polarizer. Therefore, a positive I_{dc} requires a larger current to stabilize the precession compared with the situation for negative I_{dc}. Another piece of evidence for the dual-polarizer model is the onset of incoherent emission for a positive bias at around $+300$ μA, while a negative bias provides coherent emission up to almost -400 μA. This is consistent with the polarizer assignment as well because, for positive I_{dc}, the top layer is active and is not pinned (compared with the bottom layer), and hence is relatively more vulnerable to instability, leading to such incoherent emission owing to the possible additional dynamics induced.

Figure 5 puts our study in the context of some selected achievements reported to date at room temperature and at zero bias field [20,21,23,24] or at a field less than 50 mT [3,17,39–42]. As can be seen, the study reported here has the highest zero-field emission frequency. All the results presented here are from a single device 100 nm in diameter, but qualitatively similar results have been observed in many other samples with different diameters and varying layer thicknesses. The emission provided by devices

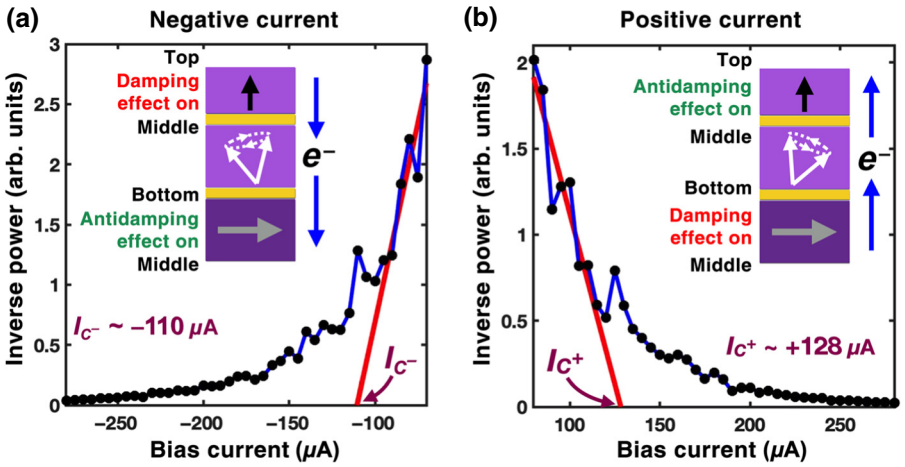

FIG. 4. Critical current for different polarities, and action of top and bottom layers on the middle layer. (a) Inverse power against negative bias current. Extrapolation of a linear fit in the subcritical regime estimates the critical current to be about −110 μA. The inset illustrates the individual roles of the top and bottom layers in the effect on the middle layer for a negative bias. (b) As (a) but for positive bias, where the critical current is estimated to be about +128 μA. As shown in the inset, the roles of the top and bottom layers are now switched.

with different middle-layer thicknesses is shown in Fig. 6, where the purple belt is included as a guide to the trend. The effective field inside the middle layer (which is the one producing the recorded emission) directly determines the emission frequency. Theoretically, a lower thickness would lead to saturation at a higher IPMA, corresponding to a higher internal field, hence maintaining the emission at a higher frequency. However, as the thickness drops below 1.42 nm, the emission frequency seems to decrease, which is possibly due to some deterioration of the quality of the film, which is only a few atomic layers thick. The device reported in this paper, which is found to have the best overall performance, is pointed out in the figure. The orange-shaded region represents the frequency window of the existing studies at zero bias field and is included for context.

Finally in Fig 7, we present some example computer-simulated oscillation trajectories for qualitative comparison with the OOP oscillation modes suggested to have been induced in the middle layer in this paper. The trajectories are generated using micromagnetic simulations using Mumax3 [43] at zero temperature according to Eqs. (1)–(3) below. Here m, m_p, B_{eff}, M_s, j_z, e, and d are the reduced free-layer magnetization, the unit vector along the polarizer, the effective magnetic field inside the free layer, the saturation magnetization of the free layer, the current density, the electronic charge, and the thickness of the free layer, respectively. Furthermore, γ_{LL}, α, p, Λ, and ε' are the gyromagnetic ratio, damping parameter, polarization efficiency, Slonczewski Λ parameter, and secondary spin-torque parameter, respectively. The equations are

$$\vec{\tau}_{\text{LL}} = \frac{\gamma_{\text{LL}}}{1+\alpha^2}\{\vec{m}\times\vec{B}_{\text{eff}} + \alpha[\vec{m}\times(\vec{m}\times\vec{B}_{\text{eff}})]\} + \vec{\tau}_{\text{SL}}, \quad (1)$$

$$\vec{\tau}_{\text{SL}} = \frac{j_z\hbar}{M_s e d}\left\{\frac{\varepsilon-\alpha\varepsilon'}{1+\alpha^2}[\vec{m}\times(\vec{m}_p\times\vec{m})] - \frac{\varepsilon'-\alpha\varepsilon}{1+\alpha^2}(\vec{m}\times\vec{m}_p)\right\}, \quad (2)$$

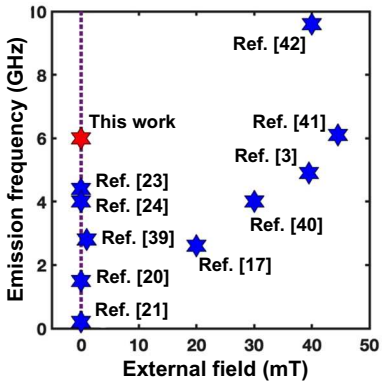

FIG. 5. Comparison of the work presented in this paper (red star) with existing studies done at room temperature at zero bias field or below 50 mT. The vertical line is a guide to the studies done at zero field.

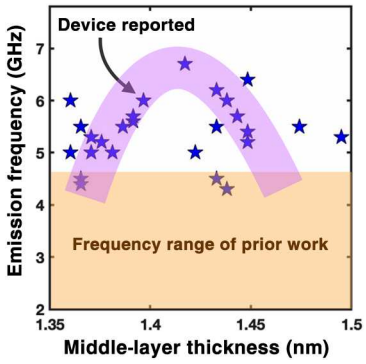

FIG. 6. Dependence of emission frequency on the thickness of the middle layer. The band shaded purple is a guide to the trend. The optimal thickness is found to be around 1.42 nm. The device reported in this paper is indicated. The area shaded in orange is the frequency window of prior studies at zero magnetic field.

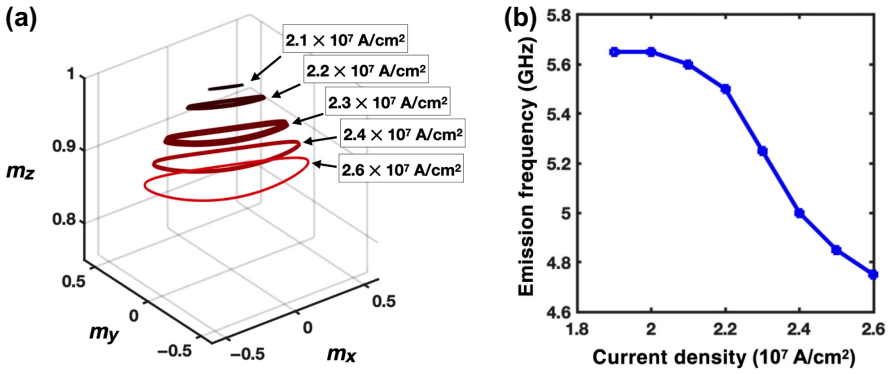

FIG. 7. Example micromagnetic simulation at zero external field. (a) OOP oscillation modes induced in a perpendicular free layer due to an in-plane fixed layer (polarizer). As the magnitude of the current is increased, the out-of-plane oscillation cone expands. (b) Redshift of peak emission frequency with current.

$$\varepsilon = \frac{p\Lambda^2}{(\Lambda^2+1)+(\Lambda^2-1)(\vec{m}\cdot\vec{m}_p)}. \tag{3}$$

The simulation is performed on a cylindrical free layer 100 nm in diameter and 1.4 nm in thickness, which is discretized into a $64 \times 64 \times 1$ mesh. In Fig. 7(a), simulated dynamics induced in a perpendicular free layer (at zero external field) due to an in-plane fixed layer (polarizer) is presented, with the simulation parameters 9.5×10^5 A/m, 2×10^{-11} J/m, 6.3×10^5 J/m^3, 0.02, 0.64, 0.8, and 0.1 for the saturation magnetization, exchange constant, uniaxial anisotropy constant, damping parameter, Λ, polarization, and secondary spin-transfer-torque term, respectively. Qualitatively similar simulated OOP modes (not shown) in a perpendicular free layer due to a perpendicular fixed layer (polarizer) are observed for the other current polarity. Figure 7(b) illustrates the frequency dependence of the magnitude of the bias current for the modes in Fig. 7(a), where the expected redshift is observed as in Fig. 2(a). The origin of this redshift in the simulation, done at zero temperature and at zero external field, is the reduction of $B_{\rm int}$ due to the reduction in m_z as the cone angle is increased.

From a practical point of view, the most interesting result of this study is the high frequency available at zero bias field. We attribute this to the dual MgO layers producing a high IPMA field inside the middle layer, which is estimated to be such that $\mu_0 H_k \sim 1.6$ T. The strength of the IPMA arising from a $Co_{20}Fe_{60}B_{20}$/MgO interface increases with decreasing $Co_{20}Fe_{60}B$ thickness but saturates below a certain thickness [30], but this saturation is overcome in this study with a second such interface. The redshift observed for both positive and negative $I_{\rm dc}$ is due to a reduction in the vertical component of the local effective field with an increase in the angle of the precession cone. A decrease in the IPMA and M_s due to Joule heating can be another reason for the inherent redshift to be enhanced. With regard to spin dynamics, the other key feature observed is the presence of bidirectional STT-induced emission. To accommodate this bidirectional emission in the STT picture, the dual roles played by the top and bottom layers are qualitatively discussed.

V. CONCLUSIONS

In summary, we demonstrate bidirectional STT-induced microwave emission from a trilayer MTJ that offers frequencies up to 6 GHz in the absence of any external field; this frequency is the highest achieved at zero field. Changes in the resistance and emission power of the MTJ are considered, to eliminate the possibility of thermally induced emission. We attribute this high frequency to the enhanced IPMA field due to the dual $Co_{20}Fe_{60}B_{20}$/MgO interfaces, and the bidirectional emission to the dual-polarizer action of the top and bottom layers. We hope that this work will promote the ongoing development of STNO-based microwave communication and neuromorphic computing.

ACKNOWLEDGMENTS

This work was supported by FAME, a STARnet center, and the NSF under Grant No. DMR-1809155. Z. M. Zeng would like to acknowledge support by the National Natural Science Foundation of China (Grant No. 51761145025).

[1] L. Berger, Emission of spin waves by a magnetic multilayer traversed by a current, Phys. Rev. B **54**, 9353 (1996).
[2] J. C. Slonczewski, Current-driven excitation of magnetic multilayers, J. Magn. Magn. Mater. **159**, L1 (1996).
[3] P. K. Muduli, O. G. Heinonen, and J. Åkerman, Bias dependence of perpendicular spin torque and of free- and fixed-layer eigenmodes in MgO-based nanopillars, Phys. Rev. B **83**, 188410 (2011).
[4] T. J. Silva and W. H. Rippard, Developments in nano-oscillators based upon spin-transfer point-contact devices, J. Magn. Magn. Mater. **320**, 1260 (2008).
[5] S. I. Kiselev, J. C. Sankey, I. N. Krivorotov, N. C. Emley, R. J. Schoelkopf, R. A. Buhrman, and D. C. Ralph, Microwave oscillations of a nanomagnet driven by a spin-polarized current, Nature **425**, 380 (2003).
[6] G. Tatara and H. Kohno, Theory of Current-Driven Domain Wall Motion: Spin Transfer Versus Momentum Transfer, Phys. Rev. Lett. **92**, 086601 (2004).
[7] Z. Zeng, G. Finocchio, and H. Jiang, Spin transfer nano-oscillators, Nanoscale **5**, 2219 (2013).

[8] Andrei N. Slavin and Pavel Kabos, Approximate theory of microwave generation in a current-driven magnetic nanocontact magnetized in an arbitrary direction, IEEE Trans. Magn. **41**, 1264 (2005).

[9] R. L. Stamps, S. Breitkreutz, J. Åkerman, A. V. Chumak, Y. Otani, G. E. W. Bauer, J.-U. Thiele, M. Bowen, S. A. Majetich, M. Kläui, I. L. Prejbeanu, B. Dieny, N. M. Dempsey, and B. Hillebrands, The 2014 magnetism roadmap, J. Phys. D: Appl. Phys. **47**, 333001 (2014).

[10] A. Makarov, T. Windbacher, V. Sverdlov, and S. Selberherr, CMOS-compatible spintronic devices: A review, Semicond. Sci. Technol. **31**, 113006 (2016).

[11] T. Chen, R. K. Dumas, A. Eklund, P. K. Muduli, A. Houshang, A. A. Awad, P. Durrenfeld, B. G. Malm, A. Rusu, and J. Akerman, Spin-torque and spin-hall nano-oscillators, Proc. IEEE **104**, 1919 (2016).

[12] A. M. Deac, A. Fukushima, H. Kubota, H. Maehara, Y. Suzuki, S. Yuasa, Y. Nagamine, K. Tsunekawa, D. D. Djayaprawira, and N. Watanabe, Bias-driven high-power microwave emission from MgO-based tunnel magnetoresistance devices, Nat. Phys. **4**, 803 (2008).

[13] A. Dussaux, B. Georges, J. Grollier, V. Cros, A. V. Khvalkovskiy, A. Fukushima, M. Konoto, H. Kubota, K. Yakushiji, S. Yuasa, K. A. Zvezdin, K. Ando, and A. Fert, Large microwave generation from current-driven magnetic vortex oscillators in magnetic tunnel junctions, Nat. Commun. **1**, 8 (2010).

[14] Z. Zeng, P. K. Amiri, I. N. Krivorotov, H. Zhao, G. Finocchio, J.-P. Wang, J. A. Katine, Y. Huai, J. Langer, K. Galatsis, K. L. Wang, and H. Jiang, High-power coherent microwave emission from magnetic tunnel junction nano-oscillators with perpendicular anisotropy, ACS Nano **6**, 6115 (2012).

[15] S. Tsunegi, K. Yakushiji, A. Fukushima, S. Yuasa, and H. Kubota, Microwave emission power exceeding 10 μW in spin torque vortex oscillator, Appl. Phys. Lett. **109**, 252402 (2016).

[16] S. Tamaru, H. Kubota, K. Yakushiji, S. Yuasa, and A. Fukushima, Extremely coherent microwave emission from spin torque oscillator stabilized by phase locked loop, Sci. Rep. **5**, 18134 (2016).

[17] D. Kumar, K. Konishi, N. Kumar, S. Miwa, A. Fukushima, K. Yakushiji, S. Yuasa, H. Kubota, C. V. Tomy, A. Prabhakar, Y. Suzuki, and A. Tulapurkar, Coherent microwave generation by spintronic feedback oscillator, Sci. Rep. **6**, 30747 (2016).

[18] P. Dürrenfeld, F. Gerhard, S. M. Mohseni, M. Ranjbar, S. R. Sani, S. Chung, C. Gould, L. W. Molenkamp, and J. Åkerman, Low-current, narrow-linewidth microwave signal generation in NiMnSb based single-layer nanocontact spin-torque oscillators, Appl. Phys. Lett. **109**, 222403 (2016).

[19] R. Lebrun, A. Jenkins, A. Dussaux, N. Locatelli, S. Tsunegi, E. Grimaldi, H. Kubota, P. Bortolotti, K. Yakushiji, J. Grollier, A. Fukushima, S. Yuasa, and V. Cros, Understanding of Phase Noise Squeezing Under Fractional Synchronization of a Nonlinear Spin Transfer Vortex Oscillator, Phys. Rev. Lett. **115**, 017201 (2015).

[20] Z. Zeng, G. Finocchio, B. Zhang, P. K. Amiri, J. A. Katine, I. N. Krivorotov, Y. Huai, J. Langer, B. Azzerboni, K. L. Wang, and H. Jiang, Ultralow-current-density and bias-field-free spin-transfer nano-oscillator, Sci. Rep. **3**, 1426 (2013).

[21] A. Dussaux, E. Grimaldi, B. Rache Salles, A. S. Jenkins, A. V. Khvalkovskiy, P. Bortolotti, J. Grollier, H. Kubota, A. Fukushima, K. Yakushiji, S. Yuasa, V. Cros, and A. Fert, Large amplitude spin torque vortex oscillations at zero external field using a perpendicular spin polarizer, Appl. Phys. Lett. **105**, 022404 (2014).

[22] B. Fang, J. Feng, H. Gan, R. Malmhall, Y. Huai, R. Xiong, H. Wei, X. Han, B. Zhang, and Z. Zeng, Zero-field spin transfer oscillators based on magnetic tunnel junction having perpendicular polarizer and planar free layer, AIP Adv. **6**, 125305 (2016).

[23] W. Skowroński, T. Stobiecki, J. Wrona, G. Reiss, and S. van Dijken, Zero-field spin torque oscillator based on magnetic tunnel junctions with a tilted CoFeB free layer, Appl. Phys. Express **5**, 063005 (2012).

[24] S. Jiang, M. Ahlberg, S. Chung, A. Houshang, R. Ferreira, P. P. Freitas, and J. Åkerman, Magnetodynamics in orthogonal nanocontact spin-torque nano-oscillators based on magnetic tunnel junctions, Appl. Phys. Lett. **115**, 152402 (2019).

[25] J. Cai, L. Zhang, B. Fang, W. Lv, B. Zhang, G. Finocchio, R. Xiong, S. Liang, and Z. Zeng, Sparse neuromorphic computing based on spin-torque diodes, Appl. Phys. Lett. **114**, 192402 (2019).

[26] D. Vodenicarevic, N. Locatelli, A. Mizrahi, J. S. Friedman, A. F. Vincent, M. Romera, A. Fukushima, K. Yakushiji, H. Kubota, S. Yuasa, S. Tiwari, J. Grollier, and D. Querlioz, Low-Energy Truly Random Number Generation with Superparamagnetic Tunnel Junctions for Unconventional Computing, Phys. Rev. Appl. **8**, 054045 (2017).

[27] M. Romera, P. Talatchian, S. Tsunegi, F. Abreu Araujo, V. Cros, P. Bortolotti, J. Trastoy, K. Yakushiji, A. Fukushima, H. Kubota, S. Yuasa, M. Ernoult, D. Vodenicarevic, T. Hirtzlin, N. Locatelli, D. Querlioz, and J. Grollier, Vowel recognition with four coupled spin-torque nano-oscillators, Nature **563**, 230 (2018).

[28] J. Torrejon, M. Riou, F. A. Araujo, S. Tsunegi, G. Khalsa, D. Querlioz, P. Bortolotti, V. Cros, K. Yakushiji, A. Fukushima, H. Kubota, S. Yuasa, M. D. Stiles, and J. Grollier, Neuromorphic computing with nanoscale spintronic oscillators, Nature **547**, 428 (2017).

[29] S. Peng, M. Wang, H. Yang, L. Zeng, J. Nan, J. Zhou, Y. Zhang, A. Hallal, M. Chshiev, K. L. Wang, and Q. Zhang, Origin of interfacial perpendicular magnetic anisotropy in MgO/CoFe/metallic capping layer structures, Sci. Rep. **5**, 18173 (2015).

[30] S. Ikeda, K. Miura, H. Yamamoto, K. Mizunuma, H. D. Gan, M. Endo, S. Kanai, J. Hayakawa, F. Matsukura, and H. Ohno, A perpendicular-anisotropy CoFeB–MgO magnetic tunnel junction, Nat. Mater. **9**, 721 (2010).

[31] See Supplemental Material at http://link.aps.org/supplemental/10.1103/PhysRevApplied.14.014040 for the experimental setup, the three-axis MR loops, the MR_Z loops at different bias currents, the emission under B_Z at different bias currents, and the correction for the impedance mismatch.

[32] M. Rickart, A. Guedes, B. Negulescu, J. Ventura, J. B. Sousa, P. Diaz, M. MacKenzie, J. N. Chapman, and P. P. Freitas, Exchange coupling of bilayers and synthetic

antiferromagnets pinned to MnPt, Eur. Phys. J. B **45**, 207 (2005).

[33] S. S. P. Parkin, N. More, and K. P. Roche, Oscillations in Exchange Coupling and Magnetoresistance in Metallic Superlattice Structures: Co/Ru, Co/Cr, and Fe/Cr, Phys. Rev. Lett. **64**, 2304 (1990).

[34] H. Kubota, A. Fukushima, Y. Ootani, S. Yuasa, K. Ando, H. Maehara, K. Tsunekawa, D. D. Djayaprawira, N. Watanabe, and Y. Suzuki, Evaluation of spin-transfer switching in CoFeB/MgO/CoFeB magnetic tunnel junctions, Jpn. J. Appl. Phys. **44**, L1237 (2005).

[35] B. Fang, M. Carpentieri, X. Hao, H. Jiang, J. A. Katine, I. N. Krivorotov, B. Ocker, J. Langer, K. L. Wang, B. Zhang, B. Azzerboni, P. K. Amiri, G. Finocchio, and Z. Zeng, Giant spin-torque diode sensitivity in the absence of bias magnetic field, Nat. Commun. **7**, 11259 (2016).

[36] H. Kubota, K. Yakushiji, A. Fukushima, S. Tamaru, M. Konoto, T. Nozaki, S. Ishibashi, T. Saruya, S. Yuasa, T. Taniguchi, H. Arai, and H. Imamura, Spin-torque oscillator based on magnetic tunnel junction with a perpendicularly magnetized free layer and in-plane magnetized polarizer, Appl. Phys. Express **6**, 103003 (2013).

[37] T. Taniguchi, S. Tsunegi, H. Kubota, and H. Imamura, Self-oscillation in spin torque oscillator stabilized by field-like torque, Appl. Phys. Lett. **104**, 152411 (2014).

[38] V. Tiberkevich, A. Slavin, and J.-V. Kim, Microwave power generated by a spin-torque oscillator in the presence of noise, Appl. Phys. Lett. **91**, 192506 (2007).

[39] O. Boulle, V. Cros, J. Grollier, L. G. Pereira, C. Deranlot, F. Petroff, G. Faini, J. Barnaś, and A. Fert, Shaped angular dependence of the spin-transfer torque and microwave generation without magnetic field, Nat. Phys. **3**, 492 (2007).

[40] D. Houssameddine, U. Ebels, B. Delaët, B. Rodmacq, I. Firastrau, F. Ponthenier, M. Brunet, C. Thirion, J.-P. Michel, L. Prejbeanu-Buda, M.-C. Cyrille, O. Redon, and B. Dieny, Spin-torque oscillator using a perpendicular polarizer and a planar free layer, Nat. Mater. **6**, 447 (2007).

[41] A. V. Nazarov, K. Nikolaev, Z. Gao, H. Cho, and D. Song, Microwave generation in MgO magnetic tunnel junctions due to spin transfer effects (invited), J. Appl. Phys. **103**, 07A503 (2008).

[42] P. K. Muduli, O. G. Heinonen, and J. Åkerman, Intrinsic frequency doubling in a magnetic tunnel junction–based spin torque oscillator, J. Appl. Phys. **110**, 076102 (2011).

[43] A. Vansteenkiste, J. Leliaert, M. Dvornik, M. Helsen, F. Garcia-Sanchez, and B. Van Waeyenberge, The design and verification of MuMax3, AIP Adv. **4**, 107133 (2014).

Supplemental Material

High-Frequency Microwave Emission of a Trilayer Magnetic Tunnel Junction in the Absence of External Magnetic Bias Field

R.N.S Rajapakse[1], Z. Zeng[2], H.W. Jiang[1]

[1]*Department of Physics and Astronomy, University of California Los Angeles, USA.*

[2]*Key Laboratory of Nanodevices and Applications, Suzhou Institute of Nano-tech and Nano-bionics, Chinese Academy of Sciences, Ruoshui Road 398, Suzhou 215123, P. R. China*

**Corresponding author - H.W. Jiang (jiangh@physics.ucla.edu)*

1. Experimental setup

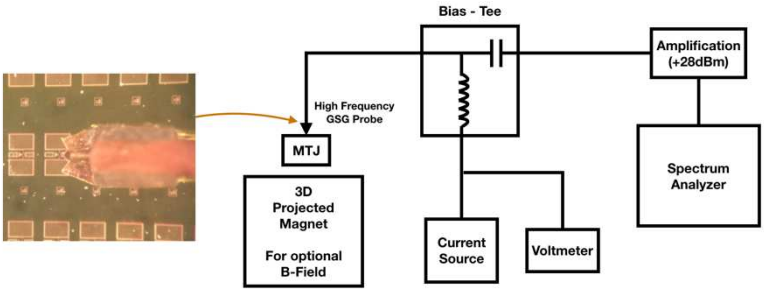

FIG. S1 - Experimental setup. On the left is the view of the GSG probe making electrical contact with the device as observed through a microscope. On the right is the schematic diagram of the setup.

2. X,Y and Z magnetoresistance loops with comparison

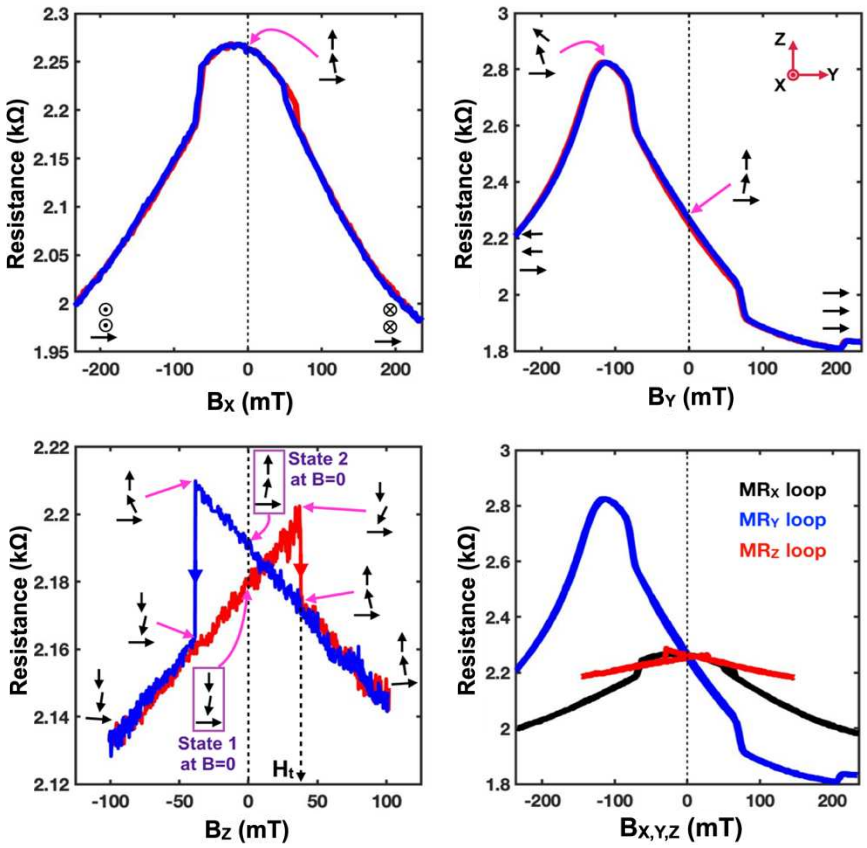

FIG. S2 - 3-axis MR Loops

All $MR_{X,Y,Z}$ loops have also been plot in one axis system for comparison. Both minimum and maximum r rence layer) is identified to

FIG. S2 - MR_X, MR_Y, MR_Z loops obtained at I_{DC}= 10 μA.

3. MR_Z loops at different bias current values

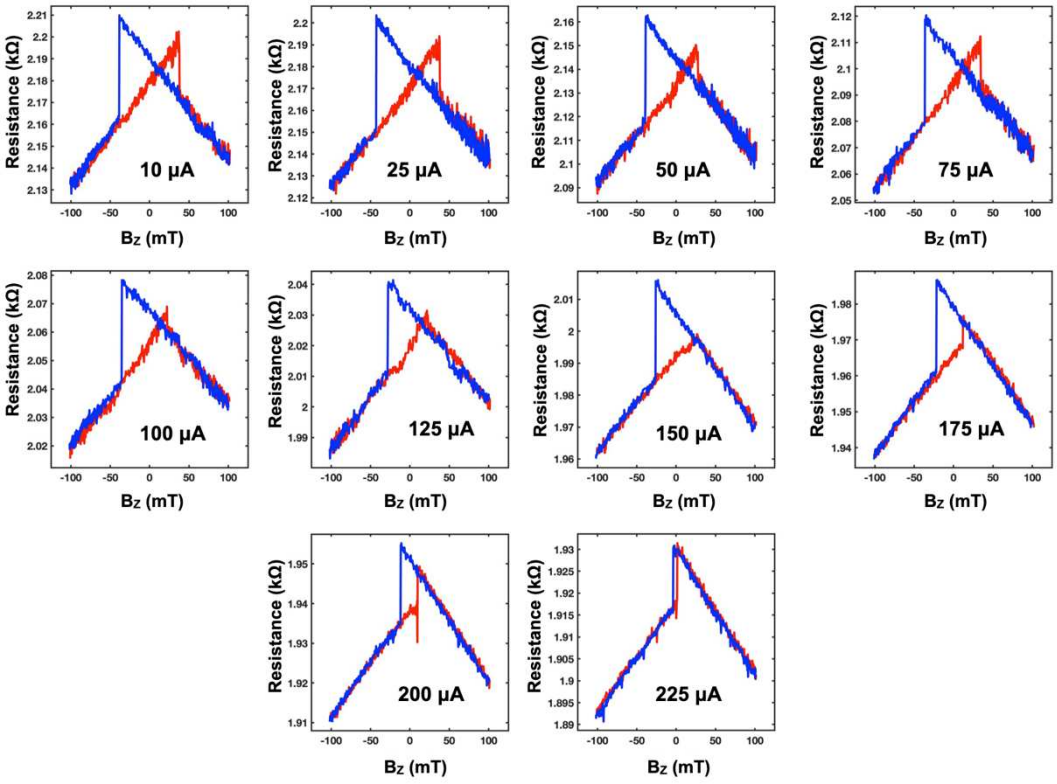

FIG. S3 - MR_Z loop at different I_{DC}.

MR_Z loop for 10 μA is presented in the main paper along with the definition of H_t , the field at which the right hand side hysteresis transition occurs. Above are MR_Z loops obtained at different I_{DC} up to 225 μA. Qualitatively they all possess two linear segments in between which two hysteresis type transitions occur. Depending on the bias current value, the location (or the field of occurrence) of the transition changes mimicking triangles or trapezoids in the curve.

4. Emission under B_Z at different I_{DC} (for state-1 initialized)

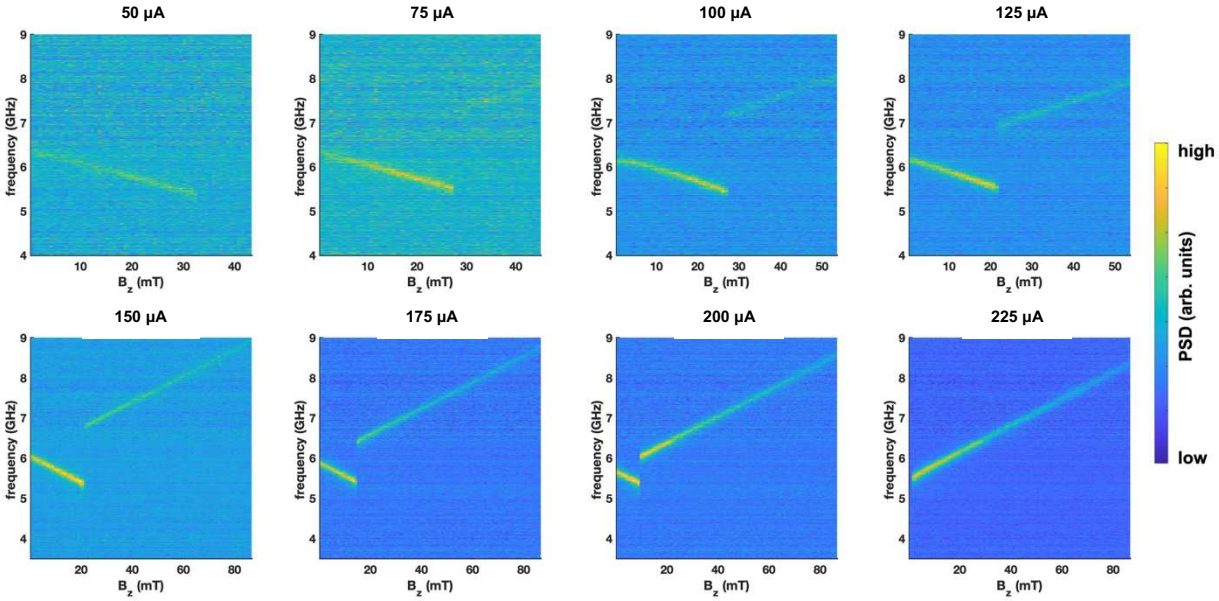

FIG. S4 - Evolution of emission at different I_{DC} upon state-1 initialization as B_Z swept in the positive direction.

Evolution of the emission with sweeping B_Z at I_{DC} = 150 μA (for both state-1 and state-2 initializations) are presented in the main paper along with the definition of H_t , the field at which the frequency discontinuity occurs for state-1 initialization. As It can be seen above, for state-1 initialization, when I_{DC} is increased, H_t decreases. At 225 μA it is found that, even for state-1 initialization (both top and middle magnetizations prepared to point downwards), STT from the bias current itself has completed the switching (as indicative by presence of only the blueshift) without any aid of an external field. This agrees well with the observation that, as I_{DC} approaches 225 μA, width of the hysteresis of MR_Z loop approaches zero.

5. Correction for impedance mismatch in emission power calculation

Device resistance has changed roughly from 2.2 kΩ to 1.7 kΩ during recording of emission (I_{DC} varied up to 400 μA). Since the impedance of the GSG probe used is 50 Ω, there is a significant impedance mismatch leading to an inefficient power transfer. For presented power, correction for this mismatch and the amplification used (28 dBm) has been accounted as follows.

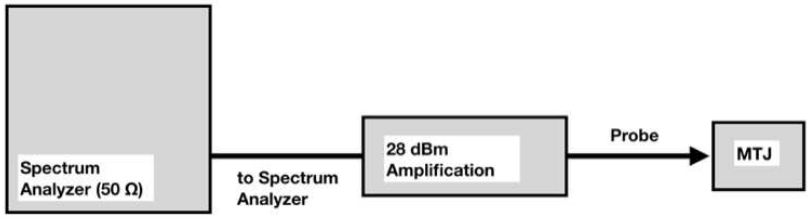

FIG. S5 - Basic experimental setup for emission measurement.

Definition of symbols

Z_{probe} = probe impedance (50 Ω)

Z_{MTJ} = MTJ impedance approximated as MTJ resistance

V_{probe} = voltage input to probe from MTJ (or voltage input to amplifier)

V_{MTJ} = microwave voltage generated from MTJ

T = MTJ to probe transmission coefficient

P_{spec} = power input to spectrum analyzer (or power output from amplifier)

P_{probe} = power input to probe from MTJ (or power input to amplifier)

P_{MTJ} = power generated from MTJ

Here Z_{MTJ} (MTJ impedance) is approximated to be MTJ resistance (R_{MTJ}) which is presented in Fig.2b in the manuscript.

Transmission coefficient for microwave voltage,

$$T = \frac{2Z_{probe}}{Z_{probe} + Z_{MTJ}}$$

$$V_{probe} = \left(\frac{2Z_{probe}}{Z_{probe} + Z_{MTJ}} \right) V_{MTJ}$$

Microwave power in MTJ and probe,

$$P_{MTJ} = \frac{V_{MTJ}^2}{Z_{MTJ}}$$

$$P_{probe} = \frac{V_{probe}^2}{Z_{probe}}$$

Combining above equations,

$$P_{probe} = \frac{4Z_{probe}Z_{MTJ}}{\left(Z_{probe} + Z_{MTJ}\right)^2} P_{MTJ}$$

Accounting for the amplification of 28 dBm,

$$P_{spec} = 10^{\frac{28}{10}} P_{probe}$$

Combining above relations, power generated at MTJ,

$$P_{MTJ} = 10^{-28/10} \frac{\left(Z_{probe} + Z_{MTJ}\right)^2}{4Z_{probe}Z_{MTJ}} P_{spec}$$